

Channel Estimation for XL-MIMO Systems with Polar-Domain Multi-Scale Residual Dense Network

Hao Lei, Jiayi Zhang, *Senior Member, IEEE*, Huahua Xiao, Xiaodan Zhang,
Bo Ai, *Fellow, IEEE*, and Derrick Wing Kwan Ng, *Fellow, IEEE*

Abstract—Extremely large-scale multiple-input multiple-output (XL-MIMO) is a promising technique to enable versatile applications for future wireless communications. In conventional massive MIMO, the channel is often modeled by the far-field planar-wavefront with rich sparsity in the angular domain that facilitates the design of low-complexity channel estimation. However, this sparsity is not conspicuous in XL-MIMO systems due to the non-negligible near-field spherical-wavefront. To address the inherent performance loss of the angular-domain channel estimation schemes, we first propose the polar-domain multiple residual dense network (P-MRDN) for XL-MIMO systems based on the polar-domain sparsity of the near-field channel by improving the existing MRDN scheme. Furthermore, a polar-domain multi-scale residual dense network (P-MSRDN) is designed to improve the channel estimation accuracy. Finally, simulation results reveal the superior performance of the proposed schemes compared with existing benchmark schemes and the minimal influence of the channel sparsity on the proposed schemes.

Index Terms—Near-field communication, XL-MIMO, channel estimation, deep learning.

I. INTRODUCTION

To significantly improve the required ultra-low access latency and ultra-high data rate of the sixth-generation (6G) wireless communications, extremely large-scale multiple-input multiple-output (XL-MIMO) has been considered as one of the promising techniques [1], [2]. The general idea of XL-MIMO is to deploy another order-of-magnitude antenna number (e.g., 512 or more) at the base station (BS), compared with only 64 or 128 antennas in those conventional massive MIMO (mMIMO) systems [1], [2]. In this way, XL-MIMO can provide higher spatial degrees-of-freedom (DoF) [1] and spectral efficiency (SE) [3] compared with mMIMO systems.

This work was supported in part by National Key R&D Program of China under Grant 2020YFB1807201, in part by National Natural Science Foundation of China under Grants 61971027 and 62221001, in part by Beijing Natural Science Foundation under Grant L202013, in part by Natural Science Foundation of Jiangsu Province, Major Project under Grant BK20212002, in part by the Key Research Projects of Universities in Guangdong Province, in 2021, under Grant 2021ZDZX1134, and in part by ZTE Industry-University-Institute Cooperation Funds under Grant No. HC-CN-20221202003. (*Corresponding author: Jiayi Zhang; Xiaodan Zhang.*)

H. Lei and J. Zhang are with the School of Electronic and Information Engineering, Beijing Jiaotong University, Beijing 100044, China (e-mail: {19211425, jiayizhang}@bjtu.edu.cn).

H. Xiao is with ZTE Corporation and State Key Laboratory of Mobile Network and Mobile Multimedia Technology. (e-mail: xiao.huahua@zte.com.cn).

X. Zhang is with School of Management, Shenzhen Institute of Information Technology, Shenzhen 518172, China (e-mail: zhangxd@szit.edu.cn).

B. Ai is with the State Key Laboratory of Rail Traffic Control and Safety, Beijing Jiaotong University, Beijing 100044, China (e-mail: boai@bjtu.edu.cn).

D. W. K. Ng is with the School of Electrical Engineering and Telecommunications, University of New South Wales, Sydney, NSW 2052, Australia (e-mail: w.k.ng@unsw.edu.au).

To achieve the desired performance in XL-MIMO networks in practice, several challenges must be addressed, e.g., accurate channel modeling, low-complexity signal processing, spatial non-stationary characteristics, etc. Among these challenges, channel estimation (CE) is a critical one as accurate channel state information (CSI) is a fundamental requirement for effective signal processing. First of all, the channel between the BS and its user equipment (UE) is with an extremely high dimensionality due to the deployment of large-scale antennas. Secondly, the operating region of XL-MIMO shifts from far-field to near-field [4], where the boundary between near-field and far-field is defined by the Rayleigh distance. With a high carrier frequency, the Rayleigh distance can be extended to hectometre-range or even longer, [4], [5], which means that XL-MIMO channels should be modeled by near-field spherical waves. The difference in electromagnetic (EM) characteristics results in different sparsity properties. Thus, the direct application of angular-domain CE schemes will inevitably suffer from a degradation in normalized mean square error (NMSE) performance for XL-MIMO [6], [7].

Recently, several works have focused on CE problems in XL-MIMO systems [6]–[11]. For instance, the authors in [6] proposed a polar-domain representation for the XL-MIMO channel that fully captures the near-field spherical wave characteristics. It is noteworthy that compressed sensing (CS) algorithms can be exploited to perform CE in XL-MIMO systems with acceptable NMSE performance based on the polar-domain channel sparsity [6]–[8]. Additionally, CS-based CE schemes have shown reasonable performance for XL-MIMO networks with spatial non-stationary properties [9], [10]. Moreover, a reduced-subspace least-squares (RS-LS) CE scheme was proposed based on the least-squares (LS) estimator by utilizing the compact eigenvalue decomposition of the spatial correlation matrix [11]. Despite various efforts have been devoted to CE, satisfactory estimation accuracy is yet to be achieved due to the limited available resources.

In recent years, deep learning (DL)-based CE algorithms have gained significant momentum. For instance, in reconfigurable intelligent surface (RIS)-aided mMIMO systems, a multiple residual dense network (MRDN) was designed for CE with high estimation accuracy by exploiting the angular-domain channel sparsity [12]. Also, the authors in [13] proposed a U-shaped multilayer perceptron (U-MLP) network to estimate the near-field channel with spatial non-stationary properties by capturing the long-range dependency of channel features. In addition, deep learning networks have been exploited to extract the parameters of near-field channels, which can be adopted to reconstruct the channel matrices [14], [15]. Moreover, the authors in [16] formulated a near-field CE

problem as a compressed sensing problem and then proposed a sparsifying dictionary learning-learning iterative shrinkage and thresholding algorithm (SDL-LISTA) by formulating the sparsifying dictionary as a neural network layer. Despite these advances, there is still a lack of sufficient investigations to reveal the impact of inherent near-field channel sparsity in different domains on DL-based CE schemes.

In this paper, we propose a polar-domain multiple residual dense network (P-MRDN)-based CE scheme to explicitly exploit the polar-domain channel sparsity in XL-MIMO systems and evaluate the NMSE performance of the MRDN and P-MRDN-based CE schemes. However, the existing DL-based CE schemes for near-field did not consider the multi-scale feature, which generally limits their accuracy. To address this issue, inspired by [17], the notion of atrous spatial pyramid pooling (ASPP), which adopts parallel atrous convolution layers with different rates to capture the multi-scale information [18], is incorporated into the proposed P-MRDN to further improve the CE accuracy. It is worth noting that our proposed schemes are expected to outperform the state-of-the-art CE schemes in NMSE due to the tailor-mode approach. The main contributions can be summarized as follows.

- We propose a P-MRDN-based CE scheme for XL-MIMO systems by exploiting the polar-domain channel sparsity. More importantly, we reveal the impact of the channel sparsity in different domains on DL-based CE schemes.
- Atrous spatial pyramid pooling-based residual dense network (ASPP-RDN) is also proposed by exploiting ASPP as a parallel branch of RDN. Then, a polar-domain multi-scale residual dense network (P-MSRDN)-based CE scheme is proposed to further improve the estimation accuracy based on ASPP-RDN.
- Numerical results demonstrate that the performance of the proposed schemes can significantly outperform existing state-of-the-art CE schemes¹.

Notation: Boldface lowercase letters \mathbf{a} and boldface uppercase letters \mathbf{A} denote column vectors and matrices, respectively. Transpose is denoted by $(\cdot)^T$. We denote the $M \times N$ complex-valued matrix and $M \times N$ real-valued matrix by $\mathbb{C}^{M \times N}$ and $\mathbb{R}^{M \times N}$, respectively. We adopt $\mathbb{E}\{\cdot\}$ to denote the expectation operator. The circularly symmetric complex Gaussian distribution with covariance σ^2 and the uniform distribution between a and b are denoted by $\mathcal{CN}(0, \sigma^2)$ and $\mathcal{U}(a, b)$, respectively. The Euclidean norm is denoted by $\|\cdot\|$.

II. SYSTEM MODEL

We consider an uplink time division duplexing (TDD) XL-MIMO system. As illustrated in Fig. 1, we consider a uniform linear array (ULA)-based BS with N antennas and one single-antenna UE for the XL-MIMO system². The antenna spacing is denoted by $\Delta = \lambda/2$, where λ is the carrier wavelength. We denote the channel between the UE and the BS by $\mathbf{h} \in \mathbb{C}^{N \times 1}$,

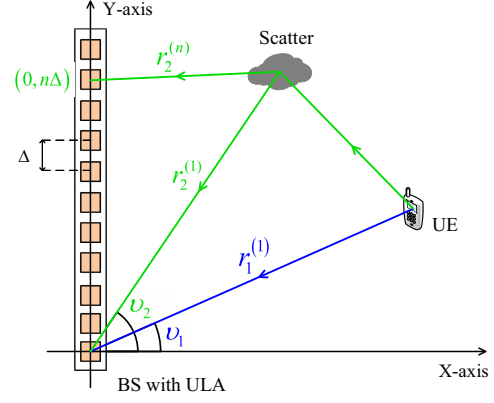


Fig. 1. Illustration of the XL-MIMO system with a uniform linear array (ULA)-based BS, where the UE and scatter are located in near-field. The figure depicts the angle v_l and the distance $r_l^{(n)}$ between the n -th BS antenna, $\forall n \in \{1, \dots, N\}$, and the scatter or the user for the l -th path, where Δ represents the antenna spacing.

where N is the number of antennas at the BS. By assuming that the UE sends a predefined pilot sequence, set as 1 for simplicity, we can represent the received signal $\mathbf{y} \in \mathbb{C}^{N \times 1}$ at the BS as

$$\mathbf{y} = \sqrt{p}\mathbf{h} + \mathbf{n}, \quad (1)$$

where p is the transmit power of the UE, $\mathbf{n} \in \mathbb{C}^{N \times 1}$ denotes the receiver noise with independent $\mathcal{CN}(0, \sigma^2)$ entries, and σ^2 denotes the noise power. To further unveil the channel sparsity in XL-MIMO, the channel modelings for far-field and near-field are reviewed as follows:

- *Far-field channel modeling:* In conventional far-field region, the channel is modeled by the planar wave, which can be expressed as

$$\mathbf{h}^{\text{far-field}} = \sqrt{\frac{N}{L}} \sum_{l=1}^L \beta_l e^{-jk r_l} \mathbf{a}(\theta_l), \quad (2)$$

where $k = \frac{2\pi}{\lambda}$ is the wave number. We assume that there is one line-of-sight (LoS) path and $L - 1$ non-line-of-sight (NLoS) paths [6]–[8]. Moreover, we denote the angle, the distance, and the complex path gain of the l -th path by $\theta_l = \sin v_l$, r_l , and β_l , respectively. The steering vector $\mathbf{a}(\theta_l)$ can be represented as

$$\mathbf{a}(\theta_l) = \frac{1}{\sqrt{N}} [1, e^{j\pi\theta_l}, \dots, e^{j(N-1)\pi\theta_l}]^T. \quad (3)$$

More interestingly, to exploit the angular-domain channel sparsity, the corresponding angular-domain representation $\mathbf{h}_A^{\text{far-field}}$ can be derived from the channel $\mathbf{h}^{\text{far-field}}$ as [6]

$$\mathbf{h}^{\text{far-field}} = \mathbf{F} \mathbf{h}_A^{\text{far-field}}, \quad (4)$$

where $\mathbf{F} = [\mathbf{a}(\theta_0), \dots, \mathbf{a}(\theta_{N-1})] \in \mathbb{C}^{N \times N}$ is the Fourier transform matrix with $\theta_n = \frac{2n-N+1}{N}$, $n = 0, 1, \dots, N-1$. Based on the angular-domain sparsity, several CS-based CE schemes have been proposed for far-field applications, e.g., [19], [20].

However, the angular-domain sparsity is not remarkable in XL-MIMO. The reason is that the Rayleigh distance, $Z = 2D^2/\lambda$, can be in the range of hectometre or longer in XL-MIMO, where D is the array aperture. For instance, the

¹Simulation codes are provided to reproduce the results in this paper: <https://github.com/BJTU-MIMO>.

²As for multi-UE scenarios, the channels between the BS and its different UEs can be modeled separately by the spherical-wave assumption.

Rayleigh distance is around 67 meters with the array aperture of 1 meters and the carrier frequency of 10 GHz. Therefore, we should consider the scenario that the UE is in near-field for XL-MIMO.

• *Near-field channel modeling*: Based on the exact spherical wave, the near-field channel can be expressed as [6]

$$\mathbf{h}^{\text{near-field}} = \sqrt{\frac{N}{L}} \sum_{l=1}^L \beta_l e^{-jk r_l} \mathbf{b}(\theta_l, r_l). \quad (5)$$

It is worth noting that the near-field steering vector $\mathbf{b}(\theta_l, r_l)$ is expressed as

$$\mathbf{b}(\theta_l, r_l) = \frac{1}{\sqrt{N}} \left[1, e^{-jk(r_l^{(2)} - r_l^{(1)})}, \dots, e^{-jk(r_l^{(N)} - r_l^{(1)})} \right]^T. \quad (6)$$

We denote the distance between the n -th BS antenna and the UE or scatter by $r_l^{(n)}$, as shown in Fig. 1. Without loss of generality, we set the coordinate of the n -th antenna as $(0, n\Delta)$ such that $r_l^{(n)} = \sqrt{(r_l^{(1)} \sqrt{1 - \theta_l^2} - 0)^2 + (r_l^{(1)} \theta_l - n\Delta)^2} = \sqrt{(r_l^{(1)})^2 + n^2 \Delta^2 - 2r_l^{(1)} \theta_l n\Delta}$, where $\theta_l = \sin \nu_l \in [-1, 1]$ denotes the spatial angle.

Note that the angular field distribution is independent of the distance under the planar-wave assumption in the far-field, as shown in (3). By contrast, the EM waves in XL-MIMO systems should be modeled by the spherical-wave assumption, showing distance-dependent angular field distribution, as shown in (6).

To fully leverage the near-field channel sparsity, a polar-domain transform matrix \mathbf{D} was proposed in [6], which is denoted by $\mathbf{D} = [\mathbf{D}_{Q_1}, \mathbf{D}_{Q_2}, \dots, \mathbf{D}_{Q_N}]$ with $\mathbf{D}_{Q_n} = [\mathbf{b}(\theta_n, r_n^1), \dots, \mathbf{b}(\theta_n, r_n^{Q_n})]$, where Q_n denotes the number of sampled distances at the sampled angle θ_n . Besides, we denote the number of all sampled distances by $Q = \sum_{n=1}^N Q_n$. Based on the matrix $\mathbf{D} \in \mathbb{C}^{N \times Q}$, the near-field channel is given by [6]

$$\mathbf{h}^{\text{near-field}} = \mathbf{D} \mathbf{h}_P^{\text{near-field}}. \quad (7)$$

Similar to the angular-domain sparsity of far-field channels, near-field channels exhibit certain sparsity in the polar domain. Thus, CE can be performed with acceptable NMSE performance based on the polar-domain channel sparsity [6]-[8].

III. PROPOSED POLAR-DOMAIN CHANNEL ESTIMATION

In this section, we introduce the MRDN, P-MRDN, and P-MSRDN for the CE in XL-MIMO systems. The MRDN architecture is introduced as the fundamental component of our proposed CE schemes. Then, we propose the P-MRDN, which can effectively exploit the polar-domain channel sparsity in XL-MIMO. In addition, we highlight the differences between the MRDN and P-MRDN caused by the channel sparsity in different domains. Finally, the proposed P-MSRDN combines the application of the MRDN and ASPP to further improve the CE accuracy.

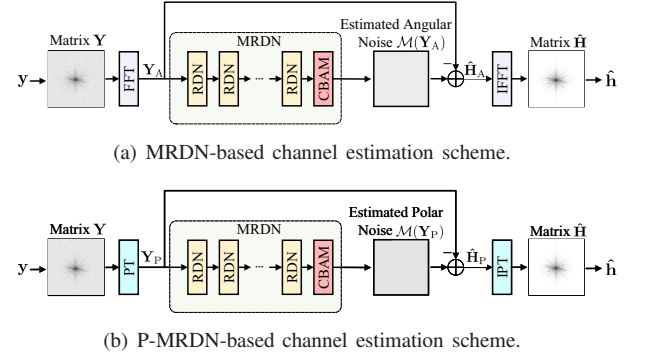


Fig. 2. Comparison between (a) MRDN-based channel estimation scheme and (b) PMRDN-based channel estimation scheme. The significant difference is the FFT in MRDN and the polar-domain transform (PT) in P-MRDN.

A. MRDN Architecture

As shown in Fig. 2 (a), residual dense network (RDN) and convolutional block attention module (CBAM) [21] are the building modules of the MRDN [12].

1) *Input Layer*: By assuming that the real and imaginary parts of the signal $\mathbf{y} \in \mathbb{C}^{N \times 1}$ are independent, we structure them into a matrix $\mathbf{Y} \in \mathbb{R}^{N \times 2}$. Thus, the matrix \mathbf{Y} can be treated as a two-dimensional image and serve as the input of our schemes.

2) *Basic Structure*: We denote *Convolution* and *Rectified Linear Units* by “Conv” and “ReLU”, respectively. “Conv” and “ReLU” layer functions are denoted by $*$ and \max , respectively. Then, as shown in Fig. 3 (a), the model of the n -th residual block is a combination of two cascaded functions:

$$\mathbf{r}_{-1} = W_{n,r} * \mathbf{x} + b_{n,r}, \quad (8)$$

$$\mathbf{r}_0 = \max(0, \mathbf{r}_{-1}), \quad (9)$$

where $\{W_{n,r}, b_{n,r}\}$, $n \in \{1, 2, \dots, M\}$, denote the weight and bias matrices, respectively. As shown in Fig. 3 (a), M is the number of layers of RDN. We denote the input and output of the residual block by \mathbf{x} and \mathbf{r} , respectively.

3) *RDN Structure*: As shown in Fig. 2 (a), in the n -th residual block, with f_n denoting the recursion function, the recurrence relation is $\mathcal{F}_1 = f_1(\mathbf{x})$ and

$$\mathcal{F}_n = f_n(\mathcal{F}_{n-1}, \dots, \mathcal{F}_1, \mathbf{x}), \forall n \in \{2, \dots, M\}. \quad (10)$$

4) *CBAM*: The recurrence relation of the CBAM is

$$\mathbf{r}_{-1} = W_{-1,c} * \mathbf{x} + b_{-1,c}, \quad (11)$$

$$\mathbf{r}_0 = \max(0, \mathbf{r}_{-1}), \quad (12)$$

$$\mathbf{r}_1 = W_{1,c} * \mathbf{r}_0 + b_{1,c}, \quad (13)$$

where $\{W_{-1,c}, b_{-1,c}, W_{1,c}, b_{1,c}\}$ are the weight and bias matrices, respectively. The input and output of the CBAM are denoted by \mathbf{x} and \mathbf{r}_1 , respectively.

5) *MRDN Structure*: Assuming that the MRDN consists of B RDNs and a CBAM, the recurrence relation of the MRDN is

$$\mathcal{F}(\mathbf{x}) = \mathcal{F}_{M,B} * \mathcal{F}_{M,B-1} * \dots * \mathcal{F}_{M,1}(\mathbf{x}), \quad (14)$$

$$\mathcal{M}(\mathbf{x}) = \mathcal{F} * C(\mathbf{x}), \quad (15)$$

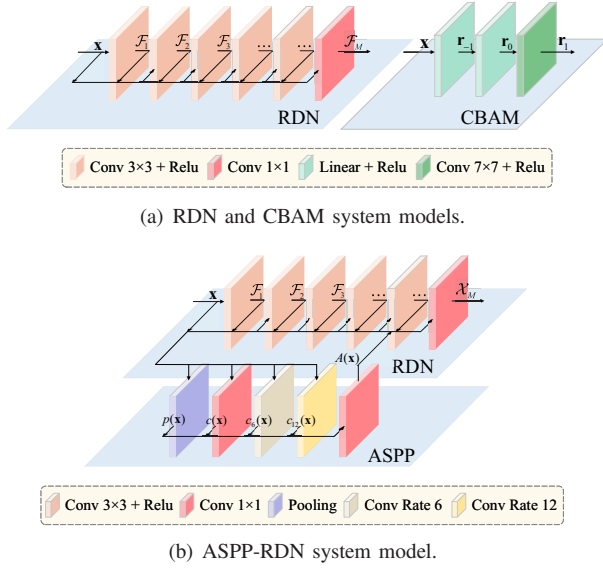


Fig. 3. Comparison between (a) RDN and CBAM system models and (b) ASPP-RDN system model. The most significant modification of ASPP-RDN is that we take advantages of ASPP as a parallel branch of RDN. The main idea for improvement is to integrate multi-scale features of its input and serve as one of the inputs of the final “Conv” layer in RDN.

where the operate \star denotes a function composition and $C(\mathbf{x})$ denotes the recursion function of the CBAM.

6) *Output Layer*: The matrix $\hat{\mathbf{H}} \in \mathbb{R}^{N \times 2}$ can produce the estimated channel $\hat{\mathbf{h}} \in \mathbb{C}^{N \times 1}$ by reversing the combining in the input layer. Besides, the loss function is given by

$$\mathcal{L} = \left\| \hat{\mathbf{h}} - \mathbf{h} \right\|^2. \quad (16)$$

B. P-MRDN-Based Channel Estimation Scheme

In conventional mMIMO systems, the operating region is far-field, i.e., the distance between the BS and the UE is longer than the Rayleigh distance. In this case, the channel can be modeled by the planar wave that solely depends on the angular information, resulting in the sparsity in the angular domain. Moreover, the angular-domain representation \mathbf{h}_A can be converted from the channel \mathbf{h} over Fast Fourier Transform (FFT), as discussed above.

As shown in Fig. 2 (a), the MRDN-based CE scheme aims to fully exploit the channel sparsity in the angular domain by transforming the matrix \mathbf{Y} into the angular domain over FFT. The estimated channel matrix $\hat{\mathbf{H}}$ is then obtained over Inverse Fast Fourier Transform (IFFT) with the matrix $\hat{\mathbf{H}}_A = \mathbf{Y}_A - \mathcal{M}(\mathbf{Y}_A)$, which can produce the estimated channel $\hat{\mathbf{h}}$.

To leverage the polar-domain channel sparsity in XL-MIMO systems, the proposed P-MRDN-based channel estimation scheme adopts the polar-domain transform (PT) to transform the matrix \mathbf{Y} to the polar domain counterpart (i.e., \mathbf{Y}_P) through the matrix \mathbf{D} , analogous to the angular domain transformation. As shown in Fig. 2 (b), the estimated channel $\hat{\mathbf{h}}$ is constructed by the estimated channel matrix $\hat{\mathbf{H}}$ which is obtained over the inverse polar-domain transform (IPT) with the matrix $\hat{\mathbf{H}}_P = \mathbf{Y}_P - \mathcal{M}(\mathbf{Y}_P)$.

Once again, the key difference between the MRDN and P-MRDN lies in their approach to exploit the inherent channel

sparsity. The MRDN-based CE scheme transforms the channel to the angular domain, exploiting the angular-domain sparsity in the far-field. In contrast, the P-MRDN-based CE scheme transforms the channel to the polar domain, leveraging the polar-domain sparsity in the near-field of XL-MIMO.

C. P-MSRDN-Based Channel Estimation Scheme

To further improve the channel estimation accuracy, we define a parallel part of the ASPP and RDN³, named ASPP-RDN, as shown in Fig. 3 (b). By incorporating the notion of ASPP into the proposed P-MRDN, the new CE scheme can achieve higher NMSE performance as the ASPP can integrate multi-scale features of its input.

1) *Atrous Spatial Pyramid Pooling Structure*: We denote the single recursion function of the pooling layer, “Conv” layer and “Conv rate = i ” layer by p , c , and c_i , respectively. Then, the recurrence relation of the ASPP can be given by

$$A(\mathbf{x}) = c(p(\mathbf{x}), c(\mathbf{x}), c_6(\mathbf{x}), c_{12}(\mathbf{x})), \quad (17)$$

where \mathbf{x} denotes the input of the ASPP, A is the mapping function for the ASPP.

2) *ASPP-RDN Structure*: Based on the ASPP and RDN structure, the recurrence relation of the proposed ASPP-RDN is

$$\mathcal{X}(\mathbf{x}) = f_M(A(\mathbf{x}), \mathcal{F}_{M-1}, \dots, \mathcal{F}_1, \mathbf{x}), \quad (18)$$

where M denotes the number of layers of the RDN and \mathbf{x} denotes the input of the ASPP-RDN.

3) *P-MSRDN Structure*: The proposed P-MSRDN jointly makes the full use of novel ideas in the ASPP and MRDN, which are illustrated as follows:

- MRDN is an extended and versatile architecture of RDN that is cascaded from multiple RDNs. The superiority of the MRDN for CE has been demonstrated due to the similarity between CE and image noise reduction. MRDN is utilized with modifications as the main component of our proposed P-MSRDN.
- ASPP has shown excellent performance in reconstructing the texture details while removing the embedded noise. We utilize the ASPP as a parallel branch of the RDN to take advantage of its multi-scale feature integration capabilities, which further enhances the accuracy of CE.
- Assuming that there are B ASPP-RDNs and a CBAM in the proposed P-MSRDN, the recurrence relation of the P-MSRDN is

$$\mathcal{Z}(\mathbf{x}) = \mathcal{X}_B \star \mathcal{X}_{B-1} \star \dots \star \mathcal{X}_1(\mathbf{x}), \quad (19)$$

$$\mathcal{Y}(\mathbf{x}) = \mathcal{Z} \star C(\mathbf{x}), \quad (20)$$

where $\mathcal{Y}: \mathbb{R}^{N \times 2} \rightarrow \mathbb{R}^{N \times 2}$ is the mapping function for the P-MSRDN. The final estimated channel $\hat{\mathbf{h}}$ can be

³By incorporating the notion of ASPP into the proposed P-MRDN-based CE scheme inspired by [17], advanced deep learning structures can be exploited to improve the performance of the proposed CE schemes. In addition, other similar structures, e.g., Encoder-Decoder and Encoder-Decoder with Atrous Conv [18], can also be employed to improve the performance of the proposed CE schemes. It is crucial to note that introducing more advanced structures is vital in optimizing the complexity, fitting, and generalization capabilities of the proposed schemes. These aspects deserve further investigation in the future.

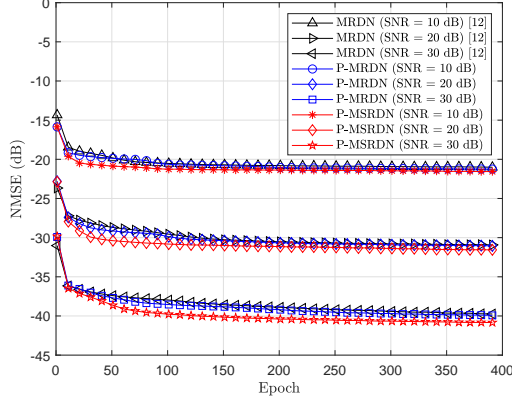


Fig. 4. Convergence of the three considered channel estimation schemes (i.e., the MRDN, P-MRDN, and P-MSRDN) under different training SNRs.

obtained by reversing the combining in the input layer, as shown in Fig. 2 (b).

D. Computational Complexity

The computational complexity of orthogonal matching pursuit (OMP) and polar-domain orthogonal matching pursuit (P-OMP) are expressed as $\mathcal{O}(L^3 N^2)$ and $\mathcal{O}(L^3 N Q)$, respectively [7]. On the other hand, the computational complexity of the running phase in the MRDN is given by [12]

$$\mathcal{O}(BMN^2 K^2 E^2), \quad (21)$$

where K^2 is the size of kernels for “Conv” layers and E denotes the number of features for the MRDN. In addition, we assume that the number of features for the P-MRDN and P-MSRDN are also E . The computational complexity of the running phase in the P-MRDN and P-MSRDN are expressed as

$$\mathcal{O}(BMNQK^2 E^2), \quad (22)$$

and

$$\mathcal{O}(B(M+4)NQK^2 E^2). \quad (23)$$

IV. SIMULATION RESULT

We consider a XL-MIMO system, where $N = 128$, $\lambda = 0.03$ meters, $L = 6$, and $Q = 256$. The complex path gain β_l and the distance r_l of the l -th path are generated as: $\beta_l \sim \mathcal{CN}(0, 1)$ and $r_l \sim \mathcal{U}(5, 50)$ meters, respectively. In terms of hardware, we implement the proposed schemes using Intel Core i7-12700, 16 GB RAM, and NVIDIA GeForce GTX 1660 SUPER through PyTorch library. The learning rate is set as 0.0001 for the MRDN, P-MRDN, and P-MSRDN. We adopt 16000 and 4000 samples for the training and testing sets of three schemes, respectively. The number of residual blocks for the RDN and the number of the RDN for our schemes are 6 and 8, respectively. Besides, the NMSE is defined as $\text{NMSE} = \mathbb{E}(\|\mathbf{h} - \hat{\mathbf{h}}\|^2 / \|\mathbf{h}\|^2)$.

The convergence performances of the proposed CE schemes are compared in Fig. 4, where the training SNRs are set to 10, 20, and 30 dB, respectively. The first observation is

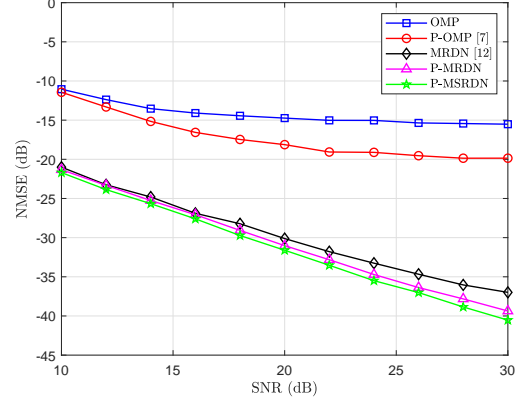


Fig. 5. NMSE performance comparison of the P-MRDN and P-MSRDN with MRDN and CS schemes.

that the proposed P-MSRDN can achieve the best NMSE performance and the fastest convergence among the considered schemes, irrespective of the training SNRs. Specifically, after 400 epochs, the performance gaps between the P-MRDN and MRDN for the training SNRs of 10, 20, and 30 dB are 0.24, 0.13, and 0.18 dB, respectively. In comparison, the performance gaps between the P-MSRDN and MRDN are 0.55, 0.63, and 1.09 dB, respectively. The reason for this improvement is that the P-MSRDN can effectively exploit the polar-domain channel sparsity and captures more features compared with the MRDN and P-MRDN. Furthermore, it is worth noting that all the schemes achieve their convergence within 300 epochs.

Fig. 5 compares the NMSE performance of our proposed schemes with the MRDN-based and CS-based schemes. OMP provides the worst NMSE performance, while P-OMP has a significantly better NMSE performance compared to OMP, with a 3.39 dB and 4.34 dB increase when the SNR is 20 dB and 30 dB, respectively. In addition, the proposed P-MRDN outperforms the MRDN by 2.38 dB when the SNR is 30 dB. These reveal the superiority of the polar-domain schemes, which can effectively exploit the rich polar-domain channel sparsity in XL-MIMO for lowering the NMSE in CE. An interesting finding is that the channel sparsity has minimal influence on the DL-based schemes compared with the CS-based schemes. The possible reason could be that the MRDN has already learned implicitly a portion of the unstructured near-field information. It is worth noting that the proposed P-MRDN provides a 12.89 dB and 19.51 dB NMSE performance gain over the P-OMP when the SNR is 20 dB and 30 dB, respectively. More importantly, the proposed P-MSRDN can achieve better NMSE performance compared to other schemes, with a gain of 1.49 dB and 3.54 dB over the MRDN when the SNR is 20 dB and 30 dB, respectively. We can also find that the NMSE performance gaps between the P-MSRDN and other schemes become larger with the increase of SNR. Indeed, the exploitation of the ASPP to capture multi-scale features of the polar-domain channel is the main reason for this improvement. Overall, the proposed P-MSRDN produces the best quality of

TABLE I
COMPARISON OF COMPUTATIONAL COMPLEXITY AND RUNNING TIME
OVER DIFFERENT CHANNEL ESTIMATION SCHEMES.

Scheme	Computational Complexity	Running Time (ms)	Ratio of Running Time
OMP	$\mathcal{O}(L^3 N^2)$	5.47	$\times 1$
P-OMP [7]	$\mathcal{O}(L^3 N Q)$	8.43	$\times 1.54$
MRDN [12]	$\mathcal{O}(B M N^2 K^2 E^2)$	4.53	$\times 0.83$
P-MRDN	$\mathcal{O}(B M N Q K^2 E^2)$	4.77	$\times 0.87$
P-MSRDN	$\mathcal{O}(B(M+4) N Q K^2 E^2)$	7.41	$\times 1.35$

In this table, N is the number of antennas for the BS; L denotes the number of all path components; $Q = 2N$ is the number of all the sampled distances for the matrix \mathbf{D} ; K^2 is the size of kernels for “Com” layers; B denotes the number of RDN for MRDN or ASPP-RDN for P-MSRDN; M is the number of layers of RDN; E denotes the number of features for “Com” layers. Besides, the running time ratios of all the schemes are calculated with respect to the one achieved by the OMP and the running time can be further shortened if tailor-mode computing devices are adopted.

CE compared to the other schemes.

The computational complexity and running time of all the schemes are compared in TABLE I. In particular, we normalize the running time of all the schemes by the one obtained by OMP for comparison. As discussed above, OMP and P-OMP achieve the lowest computational complexity at the cost of high estimation error. In addition, all the schemes have the same order of magnitude of running time. More importantly, the P-MSRDN achieves better NMSE performance compared to the MRDN and P-MRDN, but only requires a similar computational complexity. This is due to the fact that the P-MSRDN can capture the multi-scale features of the polar-domain channel through the exploitation of the ASPP.

V. CONCLUSION

We proposed the P-MRDN and P-MSRDN-based CE schemes for XL-MIMO systems, building on the conventional MRDN structure. More specifically, the proposed P-MSRDN can achieve superior generalization capabilities by utilizing several techniques, e.g., exploiting the near-field channel sparsity in the polar domain, deep residual learning, and extracting features at multi-scale resolutions. By transforming the channel into the polar domain, the proposed P-MRDN and P-MSRDN schemes can effectively exploit the sparsity in the polar domain that outperform the MRDN scheme and the conventional CS schemes. As for potential future works, the topics could be the CE for hybrid-field scenario of XL-MIMO, where various UEs are in near-field and others are in far-field.

REFERENCES

- [1] Z. Wang, J. Zhang, H. Du, W. E. I. Sha, B. Ai, D. Niyato, and M. Debbah, “Extremely large-scale MIMO: Fundamentals, challenges, solutions, and future directions,” *IEEE Wireless Commun.*, pp. 1–9, early access, 2023.
- [2] J. Zhang, E. Björnson, M. Matthaiou, D. W. K. Ng, H. Yang, and D. J. Love, “Prospective multiple antenna technologies for beyond 5G,” *IEEE J. Sel. Areas Commun.*, vol. 38, no. 8, pp. 1637–1660, Aug. 2020.
- [3] H. Lei, Z. Wang, H. Xiao, J. Zhang, and B. Ai, “Uplink performance of cell-free extremely large-scale MIMO systems,” *arXiv:2301.12086*, 2023.
- [4] J. Yang, Y. Zeng, S. Jin, C. K. Wen, and P. Xu, “Communication and localization with extremely large lens antenna array,” *IEEE Trans. Wireless Commun.*, vol. 20, no. 5, pp. 3031–3048, May 2021.
- [5] P. Ramezani and E. Björnson, “Near-field beamforming and multiplexing using extremely large aperture arrays,” *arXiv:2209.03082*, 2022.
- [6] M. Cui and L. Dai, “Channel estimation for extremely large-scale MIMO: Far-field or near-field?” *IEEE Trans. Commun.*, vol. 70, no. 4, pp. 2663–2677, Apr. 2022.
- [7] X. Wei and L. Dai, “Channel estimation for extremely large-scale massive MIMO: Far-field, near-field, or hybrid-field?” *IEEE Commun. Lett.*, vol. 26, no. 1, pp. 177–181, Jan. 2022.
- [8] X. Zhang, H. Zhang, and Y. C. Eldar, “Near-field sparse channel representation and estimation in 6G wireless communications,” *arXiv:2212.13527*, 2022.
- [9] Y. Han, S. Jin, C. K. Wen, and X. Ma, “Channel estimation for extremely large-scale massive MIMO systems,” *IEEE Wireless Commun. Lett.*, vol. 9, no. 5, pp. 633–637, May 2020.
- [10] Y. Zhu, H. Guo, and V. K. N. Lau, “Bayesian channel estimation in multi-user massive MIMO with extremely large antenna array,” *IEEE Trans. Signal Process.*, vol. 69, pp. 5463–5478, Sep. 2021.
- [11] Ö. T. Demir, E. Björnson, and L. Sanguinetti, “Channel modeling and channel estimation for holographic massive MIMO with planar arrays,” *IEEE Wireless Commun. Lett.*, vol. 11, no. 5, pp. 997–1001, May. 2022.
- [12] Y. Jin, J. Zhang, C. Huang, L. Yang, H. Xiao, B. Ai, and Z. Wang, “Multiple residual dense networks for reconfigurable intelligent surfaces cascaded channel estimation,” *IEEE Trans. Veh. Technol.*, vol. 71, no. 2, pp. 2134–2139, Feb. 2022.
- [13] J. Xiao, J. Wang, Z. Chen, and G. Huang, “U-MLP based hybrid-field channel estimation for XL-RIS assisted millimeter-wave MIMO systems,” *IEEE Wireless Commun. Lett.*, pp. 1–1, early access, 2023.
- [14] Y. Chen, L. Yan, and C. Han, “Hybrid spherical- and planar-wave modeling and DCNN-powered estimation of terahertz ultra-massive MIMO channels,” *IEEE Trans. Commun.*, vol. 69, no. 10, pp. 7063–7076, Oct. 2021.
- [15] A. Lee, H. Ju, S. Kim, and B. Shim, “Intelligent near-field channel estimation for terahertz ultra-massive MIMO systems,” in *Proc. 2022 IEEE Glob. Commun. Conf. (GLOBECOM)*, Dec. 2022, pp. 5390–5395.
- [16] X. Zhang, Z. Wang, H. Zhang, and L. Yang, “Near-field channel estimation for extremely large-scale array communications: A model-based deep learning approach,” *IEEE Commun. Lett.*, vol. 27, no. 4, pp. 1155–1159, Apr. 2023.
- [17] L. Bao, Z. Yang, S. Wang, D. Bai, and J. Lee, “Real image denoising based on multi-scale residual dense block and cascaded U-Net with block-connection,” in *Proc. IEEE CVF Conf. Comput. Vis. Pattern Recognit. Workshops*, 2020, pp. 448–449.
- [18] L. C. Chen, Y. Zhu, G. Papandreou, F. Schroff, and H. Adam, “Encoder-decoder with atrous separable convolution for semantic image segmentation,” in *Proc. Eur. Conf. Comput. Vis.*, 2018, pp. 801–818.
- [19] J. Lee, G. T. Gil, and Y. H. Lee, “Channel estimation via orthogonal matching pursuit for hybrid MIMO systems in millimeter wave communications,” *IEEE Trans. Commun.*, vol. 64, no. 6, pp. 2370–2386, Jun. 2016.
- [20] C. Huang, L. Liu, C. Yuen, and S. Sun, “Iterative channel estimation using LSE and sparse message passing for mmWave MIMO systems,” *IEEE Trans. Signal Process.*, vol. 67, no. 1, pp. 245–259, Jan. 2019.
- [21] S. Woo, J. Park, J. Y. Lee, and I. S. Kweon, “CBAM: Convolutional block attention module,” in *Proc. Eur. Conf. Comput. Vis.*, 2018, pp. 3–19.